Statistical Study of Electron Density Enhancements in the Ionospheric *F* Region Associated with Pulsating Auroras

M. Fukizawa[1], T. Sakanoi[1], Y. Ogawa[2], T. T. Tsuda[3], and K. Hosokawa[3]

[1] Graduate School of Science, Tohoku University, Sendai, Japan

[2] National Institute of Polar Research, Tachikawa, Japan

[3] Graduate School of Informatics and Engineering, University of Electro-Communications, Chofu, Japan

Corresponding author: Mizuki Fukizawa (fukizawa.m@pparc.gp.tohoku.ac.jp)

Key Points:

- Seventy-six percent of the electron density height profiles during pulsating auroras had a local enhancement in the ionospheric *F* region.
- The occurrence rate of these profiles exceeded 80% in 22–3 magnetic local time.
- Eighty-nine percent of the *F* region peak altitudes were above the peak altitude of the ionization rate produced by 100 eV electrons.

Abstract

Pulsating auroras (PsAs) are considered to be caused by energetic (~10 keV) electron precipitations. Additionally, soft electron precipitations (~1 keV) have often been observed in PsAs. These soft electron precipitations enhance the electron density in the ionospheric *F* region. However, to date, the relationship between PsAs and soft electron precipitation has not been well understood. In this study, using the data taken by the European incoherent scatter radar and the auroral all-sky imager at Tromsø, we conducted two case studies to investigate, in detail, the relationship between the electron density height profile and the type of aurora. Additionally, we conducted statistical studies for 14 events to elucidate how often *F* region electron density enhancement occurs with a PsA. We consequently found that 76% of electron density height profiles showed a local peak in the *F* region, with electron temperature enhancements. It was also found that 89% of the *F* region peak altitudes were above the peak altitude of the ionization rate produced by electrons of characteristic energy below 100 eV. The occurrence rate of these profiles in the hourly magnetic local time (MLT) exceeded 80% in the 22–3 MLT sectors. We suggest that the electron density enhancement in the *F* region would have been caused by electrostatic electron cyclotron harmonic waves in the magnetosphere. Another candidate would have been polar patches that had traveled from the dayside ionosphere.

1 Introduction

When a substorm occurs, various plasma waves are excited in the inner magnetosphere by temperature anisotropies and loss cone distribution of the plasma injected from the magnetospheric tail. Immediately after auroral breakups, auroras start to blink quasi-periodically on a time scale of a few seconds to tens of seconds (Yamamoto, 1988). These auroras, called pulsating auroras (PsAs), are believed to be driven by precipitating electrons above a few kiloelectron volts that are scattered into a loss cone through cyclotron resonance with lower band chorus (LBC) waves near the magnetic equator (e.g., Kasahara et al., 2018; Nishimura et al., 2010).

Sounding rockets and low-altitude satellites have typically observed pulsations in the precipitating electrons above a few kiloelectron volts, as well as stable precipitations at ~1 keV (e.g., McEwen et al., 1981; Miyoshi et al., 2015; Sandahl et al., 1980). The generation process of soft electron precipitations in the region of PsAs is considered to be the backscattering of primary and secondary electrons in the opposite hemisphere and/or pitch angle scattering by upper band chorus (UBC) waves near the magnetic equator (Evans et al., 1987; Inan et al., 1992; Miyoshi et al., 2015).

Electrostatic electron cyclotron harmonic (ECH) waves are frequently excited near the magnetic equator, and they can also scatter electrons into loss cones typically below a few kiloelectron volts (e.g., Horne et al., 2003). Fukizawa et al. (2018) reported an event that temporal modulations of LBC and ECH wave amplitudes, observed by the Exploration of energization and Radiation in Geospace (ERG) satellite, correlated with those of the pulsating auroral emission intensity observed by an all-sky imager close to the footprint of the ERG satellite and showed that the PsAs, correlated with LBC and ECH waves, were caused by ~22–76 and ~3–4 keV electrons, respectively. The soft electron precipitation would have been generated by UBC waves rather than ECH waves because the pitch angle range over which ECH waves can resonate is narrower than that of UBC waves (Tao et al., 2011; Thorne et al., 2013).

Soft electron precipitation is important since it contributes to the background diffuse auroral emission and the ionization in the ionospheric *F* region, and PsAs are typically accompanied by soft electron precipitation, as well as high-energy electron precipitation (Saito et al., 1992; Sandahl et al., 1980; Smith et al., 1980; Whalen et al., 1971). Oyama et al. (2014) reported that the ionospheric electron density had a large peak in the ionospheric *E* region, and a small peak in the ionospheric *F* region, at the beginning of the substorm recovery phase, on the basis of statistical analysis using the data taken by the European incoherent scatter (EISCAT) ultrahigh frequency (UHF) radar at Tromsø, Norway, and the International Monitor for Auroral Geomagnetic Effects magnetometer network. The *E* region peak would have been caused by the energetic electron precipitation associated with PsAs since PsAs are frequently observed in the substorm recovery phase. They attributed the enhancement of the *F* region electron density to lower energy electron precipitations and/or long-lived plasma that drifted horizontally from the dayside.

The ionospheric electron heating associated with PsAs was also observed by the Swarm satellite, and the soft electron precipitation may have had some effects (Liang et al., 2018). By contrast, Samara et al. (2015) reported that the soft electron precipitation was reduced during strongly temporally varying PsAs and attributed this reduction to the field-aligned current with parallel potential drops of up to 1 kV. It has not yet been well understood whether or not soft electron precipitation is commonly observed in PsAs. In this study, we aim to elucidate the characteristics of the soft electron precipitation in PsAs using the ionospheric electron density altitude profiles obtained with the EISCAT radar, when PsAs were observed by the all-sky imager.

We conducted the case study for two events to investigate, in detail, the relationship between the electron density height profile and the type of aurora (Section 3). Additionally, we conducted the statistical analysis for 14 events to elucidate the characteristics of the *F* region ionization in PsAs (Section 4).

2 Instrumentation

2.1 All-sky imagers

We used two Watec Monochromatic Imagers (WMIs) at Tromsø, Norway (69.58°N, 19.23°E, 66.40° magnetic latitude (MLAT)); these consisted of a highly sensitive camera with a charge-coupled device made by Watec Co. Ltd, a fish-eye lens by Fujinon Co. Ltd., two band-pass filters with center wavelengths of 560 and 632 nm, respectively, and the full width at half the maximum of 10 nm (Ogawa et al., 2020). The WMI with the band-pass filter centering at a wavelength of 560 nm was used to detect PsAs that were dominated by the green color at OI 558 nm, of which the typical altitude was in the *E* region; thus, the green line emission was used as an indicator of relatively high-energy electron precipitations. The temporal resolution was 1 s, and this was sufficient to identify the main modulation of the PsAs whose typical quasi-periodicity was from a few seconds to tens of seconds. The WMI with the band-pass filter centering at a wavelength of 632 nm was used to detect the auroral red line emission at OI 630 nm in the *F* region that was caused by the soft electron precipitation. The temporal resolution was 4 s. Hereafter, we call these two WMIs the WMI-558 and the WMI-630, respectively.

2.2 Radar

The EISCAT UHF radar that measures electron density, electron and ion temperature, and ion velocity along the beam direction has been installed at Tromsø, Norway (Folkestad et al., 1983). We used the electron density and electron temperature data obtained when the beam was directed in the local geomagnetic field-aligned direction in the altitude range of 76–282 or 76–647 km. The altitude resolution, which depended on the altitude, was 3–33 km. The temporal resolution was 1 min.

3 Case Study

3.1 Case 1: 0–4 UT on February 18, 2018

Figures 1a and 1b show the keograms obtained from the cross-section of successive all-sky images with WMI-558 and WMI-630. We selected the cross-section along the geographic north–south direction to involve a pixel of the EISCAT radar observation point. After the auroral breakup at 00:10 UT, the following three types of auroras were observed: amorphous PsAs from 00:11 to 00:20 UT (time A in Figure 1), auroral streamers from 00:31 to 00:34 UT (time B in Figure 1), and patchy PsAs from 00:46 to 03:00 UT (time C in Figure 1). The amorphous PsA is an irregularly shaped and rapidly varying PsA, and the patchy PsA comprises steady emission structures with pulsations over a large fraction of their spatial extent (Grono & Donovan, 2018). The movie of successive all-sky images for the entire time period in Figure 1 is available in Movie S1. Figures 1c–1f show the 558 and 630 nm emission intensities, electron density, and

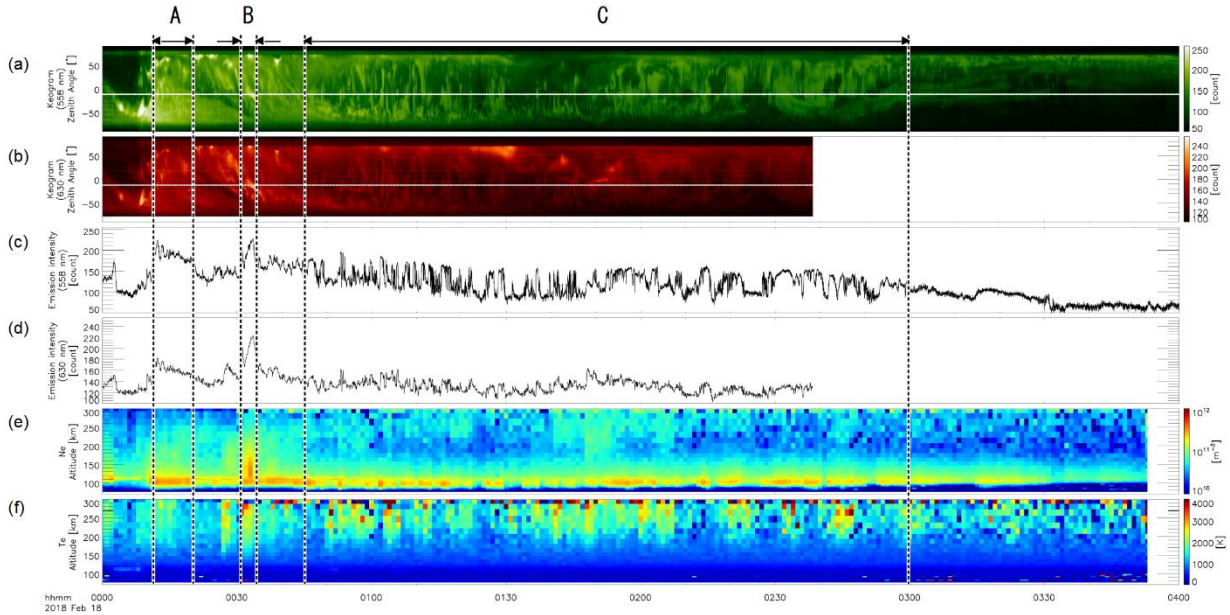

Figure 1 Keograms for **(a)** WMI-580 and **(b)** WMI-630. The horizontal dashed lines in (a) and (b) represent the pixel that corresponds to the EISCAT radar observation point. The emission intensities at the horizontal lines for **(c)** WMI-558 and **(d)** WMI-630. **(e)** electron density and **(f)** temperature obtained with the EISCAT UHF radar. Three types of aurora (amorphous PsA, auroral streamer, and patchy PsA) were mainly observed in the timespans labeled as A, B, and C.

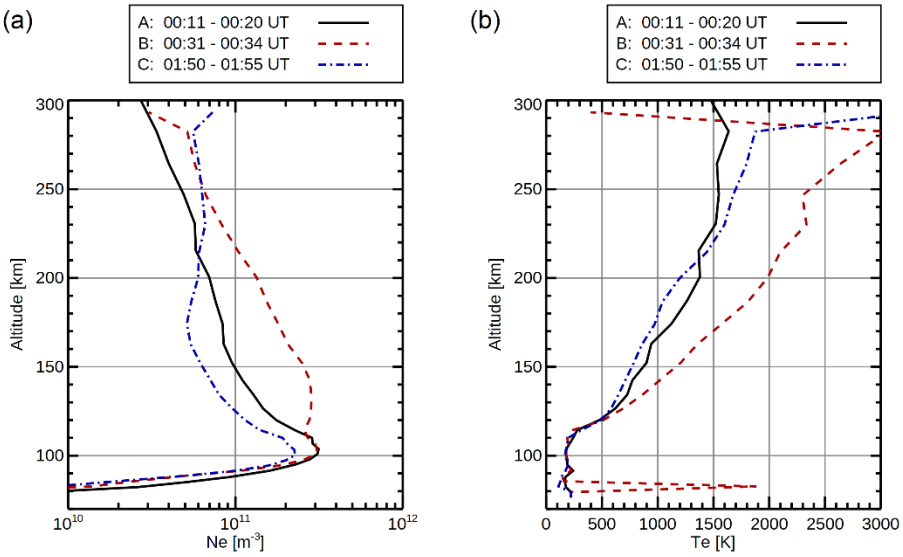

Figure 2 Height profiles of **(a)** the electron density and **(b)** temperature averaged in the timespan shown in Figure 1 as A, B, and C.

temperature at the EISCAT observation point. The electron density had a peak at an altitude of ~100 km when a discrete aurora appeared (time A in Figure 1e). The electron density at ~130 km altitude was also enhanced with the auroral streamer (time B in Figure 1e). When the 558 nm auroral emission started quasi-periodic modulations (time C in Figures 1a and 1c), the electron density at ~200 km altitude was decreased and a weak peak at ~250 km altitude emerged (Figure 1e). This double-peak structure was consistent with that reported by Oyama et al. (2014). The height profiles of the electron density and temperature averaged for the periods of A, B, and C are shown in Figures 2a and 2b, respectively. For time C, the median profile was derived for the timespan from 01:50 to 01:55 UT, when the *F* region electron density was especially enhanced. These electron density enhancements in the *E* region were probably caused by electron precipitations since they were followed by electron temperature enhancements (see Figures 1f and 2b).

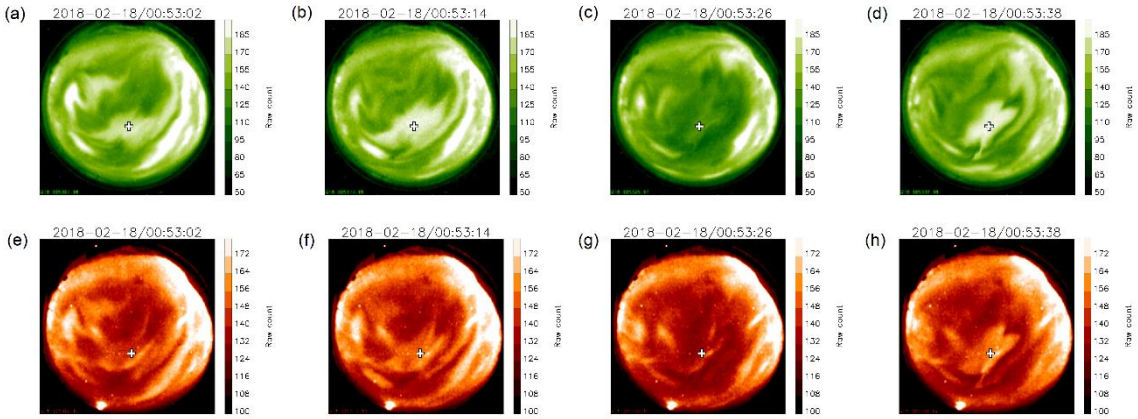

Figure 3 Successive all-sky images obtained by WMI-580 **(a–d)** and by WMI-630 **(e–h)** with a time interval of 12 seconds from 00:53:02 to 00:53:38 UT on 18 February 2018.

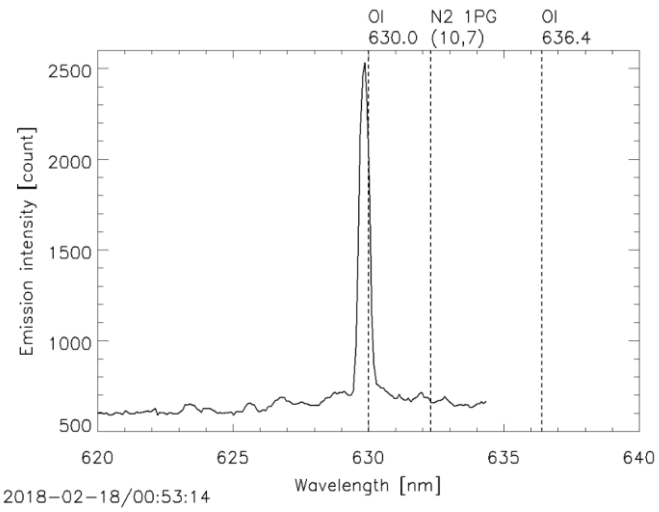

Figure 4 Auroral spectrum obtained with the compact optical spectrograph at 00:53:14 UT on 18 February 2018. It should be noted that the exposure time was 29.0 seconds, the wavelength resolution was ~0.4 nm, and the wavelength interval was ~0.1 nm.

To examine the relationship between the electron density enhancement in the *F* region and the characteristic energy of the precipitating electrons, we compared the auroral emissions at 558 nm with those at 630 nm. Figure 3 shows successive auroral images at 558 (top row) and 630 nm (bottom row) with a time interval of 12 s from 00:53:02 to 00:53:38 UT at the beginning of time C, when the on–off modulation of the auroral emission was detected. The 558 nm PsA's patch brightened at the EISCAT radar observation point, indicated by a white plus mark in Figs 3a, 3b, and 3d. The 630 nm PsA's patch, whose shape was similar to that of the 558 nm PsA, also brightened, as shown in Figures 3f and 3h. Regarding the WMI-630-observed PsAs, this type of on–off modulation (or main pulsation) could have been mainly dominated by N_2 1 PG (10,7) (not by OI 630 nm), as suggested by Tsuda et al. (2020). By contrast, their observations also showed OI 630 nm emission as a component of the stable or background emission (or the not-pulsating component). Here, Figure 4 shows the auroral spectrum obtained by a compact optical spectrograph (cf. Oyama et al., 2018; Tsuda et al., 2020) at Tromsø at the same time as that in Figure 3 when a PsA occurred. We confirmed that the 630 nm emission was obviously detected using the spectrograph. The observed OI 630 nm emission may have been due to a stable or background component. This supports the existence of the soft electron precipitation (at least as a stable or background component) during the appearance of a PsA. It is generally strange for OI 630 nm emissions to pulsate, as shown in Figures 3e–h, since their lifetime is 110 s. The OI 630 nm pulsation might have been caused at a lower altitude than a typical emission altitude by quasi-periodic soft electron precipitations, as suggested by Liang et al. (2016). Further analysis, such as that conducted by Tsuda et al. (2020), is necessary to identify which OI 630 nm emission or N_2 1 PG (10,7) emission contributed to the pulsation detected by the WMI-630, in future work.

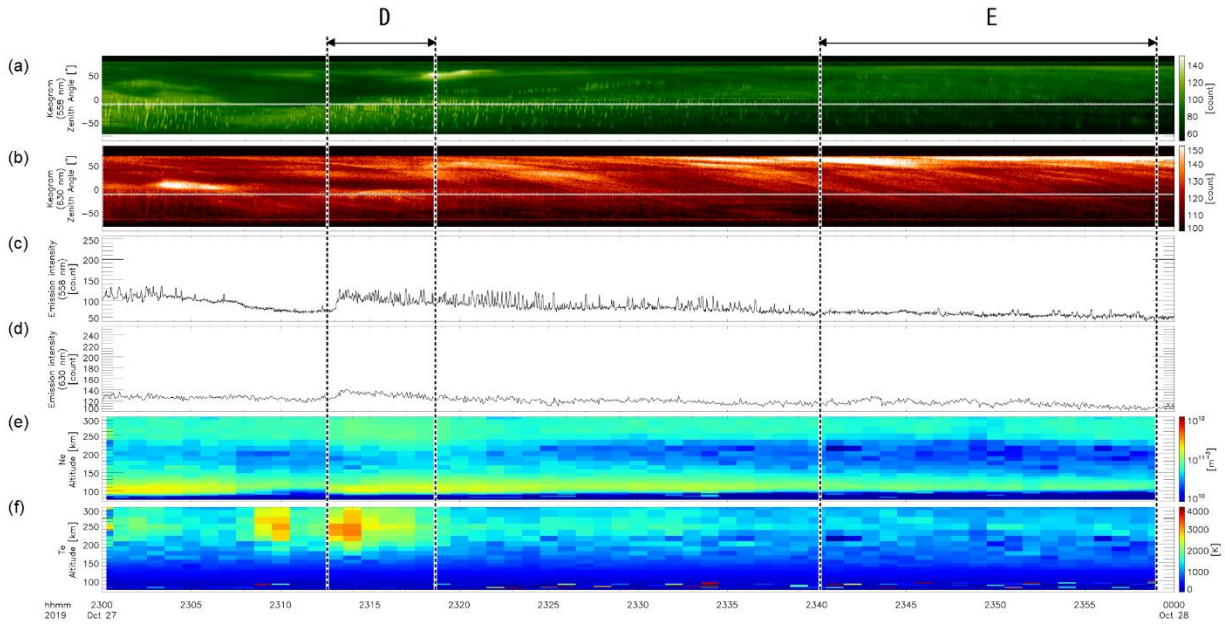

Figure 5 Keograms for **(a)** WMI-580 and **(b)** WMI-630. The emission intensities at the horizontal lines in (a) and (b) for **(c)** WMI-558 and **(d)** WMI-630. **(e)** Electron density and **(f)** temperature obtained with the EISCAT UHF radar. The electron density had a local peak in the *F* region with PsAs in the timespans labeled as D and without PsAs in the timespan labeled as E.

3.2 Case 2: 23–24 UT on October 27, 2019

Figure 5 shows observation data obtained on October 27, 2019, given in the same format as that in Figure 1. The EISCAT radar observation was conducted from 23 UT on this day. PsA patches

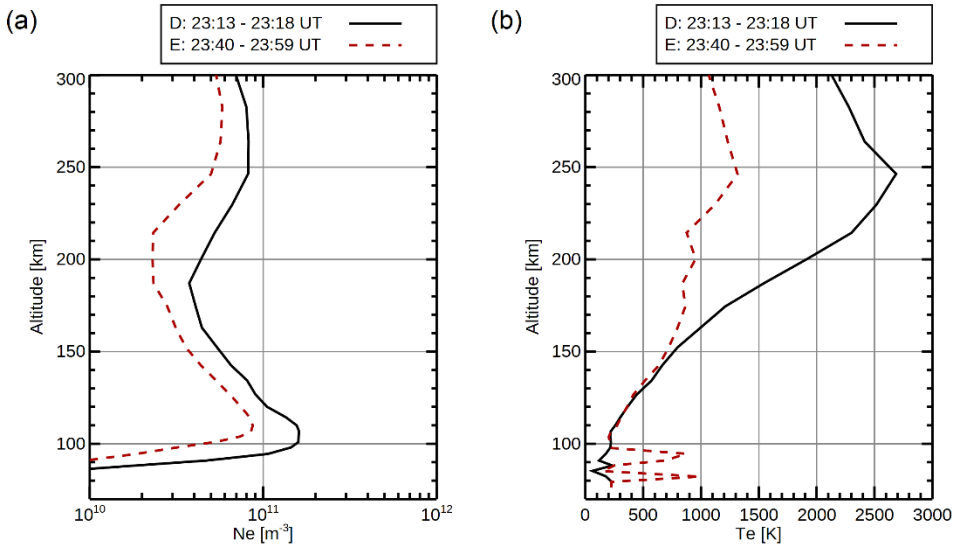

Figure 6 Height profiles of **(a)** the electron density and **(b)** temperature averaged in the timespan shown in Figure 5 as D and E.

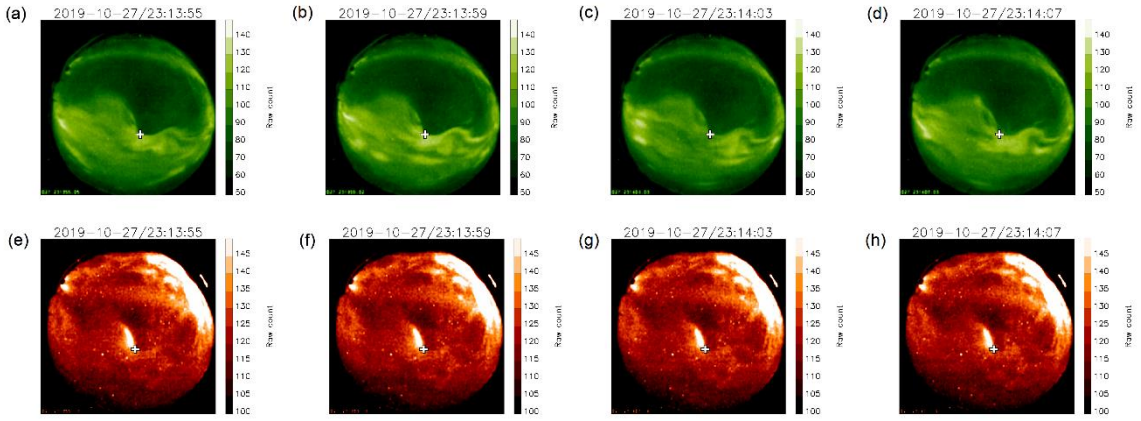

Figure 7 Successive all-sky images obtained by WMI-580 **(a–d)** and by WMI-630 **(e–h)** with a time interval of 4 seconds from 23:13:55 to 23:14:07 UT on 27 October 2019.

were detected by WMI-558 from 23:00 to 23:40 UT (Figures 5a and 1c). The movie of the all-sky images for the whole period of Figure 5 is available in Movie S2. In the 558 nm all-sky image data from 23:13 to 23:18 UT (time D in Figure 5), PsA patches were detected at the EISCAT radar observation point, and, simultaneously, the electron density in the *F* region was slightly enhanced (see Figure 5e). The height profiles of the electron density and temperature averaged for the period of D are shown with solid black lines in Figures 6a and 6b. The electron density enhancement in the *F* region was possibly caused by the soft electron precipitation since it was accompanied by both a 630 nm aurora and an electron temperature enhancement (Figures 5b, 5d, 5f, and 6b). Note that the auroral emission was partially covered by clouds moving from north to south (Figures 5a and 5b). Figure 7 shows successive auroral images with a time interval of 4 s from 23:13:55 to 23:14:07 UT. Regarding the EISCAT observation point indicated by the white plus mark, the 558 nm emission brightened, as shown in Figures 7b and 7d, whereas the 630 nm emission was somewhat stable. We confirmed that the auroral spectrum included the OI-630.0 nm emission line by the spectrograph (Figure 8). From 23:40 to 23:59 UT (time E in

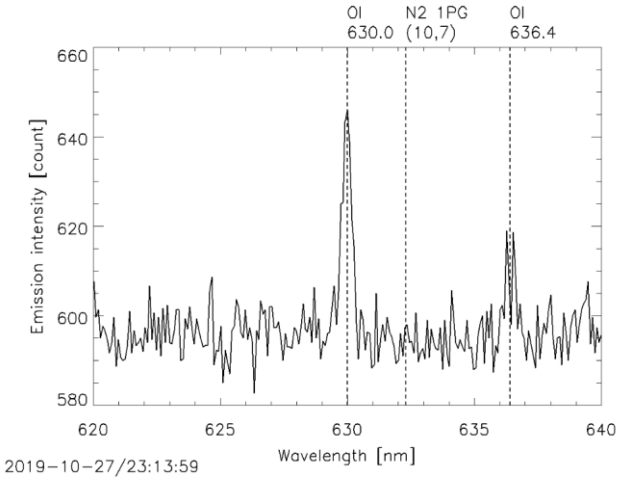

Figure 8 Auroral spectrum obtained with the compact optical spectrograph at 23:13:59 UT on 27 October 2019. It should be noted that the exposure time was 0.7 seconds, the wavelength resolution was ~0.4 nm, and the wavelength interval was ~0.1 nm.

Figure 5), the electron density in the *F* region increased (Figure 5e), whereas PsA patches were not detected at the EISCAT radar observation point (Figures 5a and 5c). The height profiles of the electron density and temperature averaged during the period of E are shown with red dashed lines in Figures 6a and 6b. This *F* region electron density peak might have been caused by polar patches since it was not accompanied by an electron temperature enhancement (Figures 5f and 6b).

4 Statistical Results

To understand the quantitative characteristics of the *F* region electron density enhancement associated with PsAs, we undertook statistical analysis using the simultaneous data with the EISCAT UHF radar with all-sky imagers for 14 nights from September 2016 to December 2019,

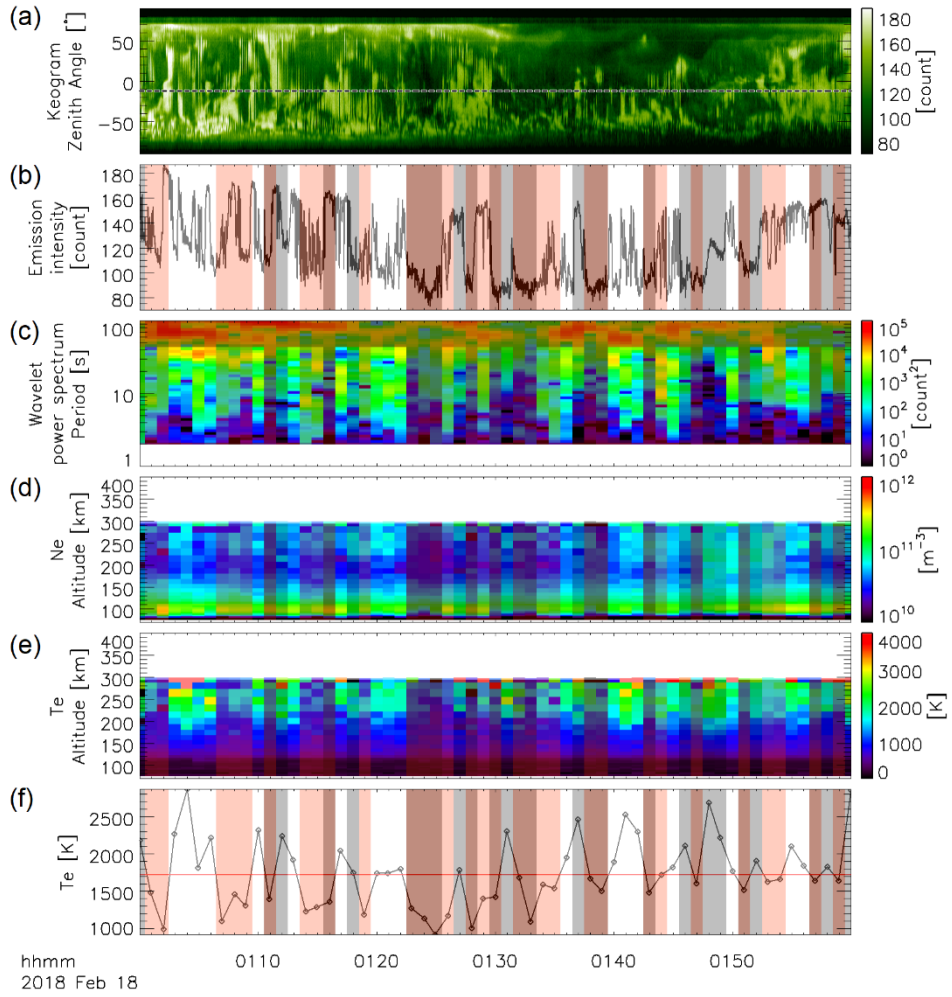

Figure 9 An example showing the procedure to extract electron-density data during PsAs with electron-temperature enhancement. **(a)** Keogram for WMI-580. **(b)** Emission intensity at the EISCAT radar observation point (horizontal dashed line in (a)). **(c)** The wavelet power spectrum of (b). **(d)** Electron density and **(e)** temperature. (f) Median electron temperature at 240–270 km altitude (black diamond and line) and its median value during an hour (red line). The gray and red shades are explained in the text.

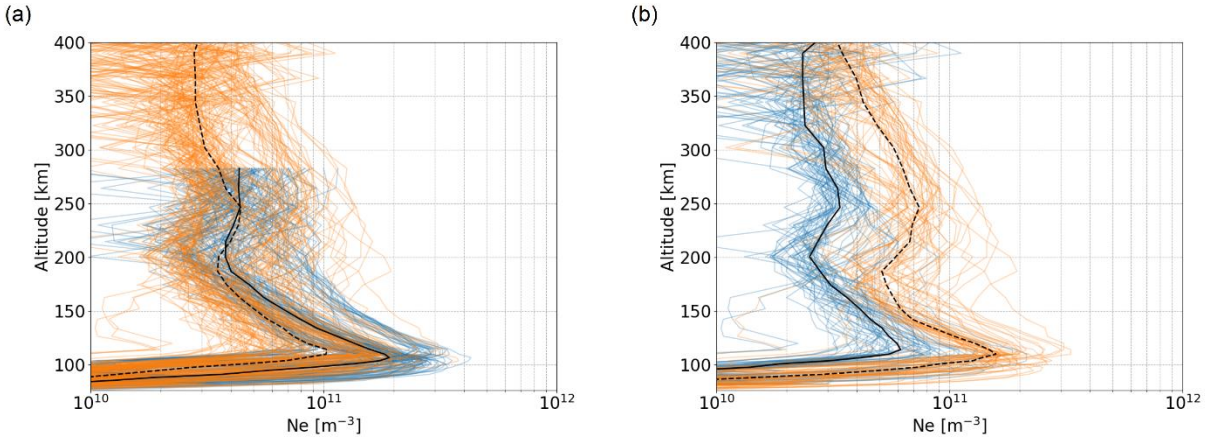

Figure 10 (a) Electron-density height profiles extracted by the procedure explained in Figure 9 for two observation modes of the EISCAT radar; one covered the altitude range from 76 to 282 km (blue lines), another mode covered the higher altitude range from 76 to 647 km (orange lines). Each median profile is shown by a solid black or dashed line. **(b)** The electron-density height profiles, which had two peaks, are shown in Figure 10a with orange lines. They are divided into two cases; one with a weak ($\leq 5 \times 10^{10}$ m^{-3}) ionization (blue lines) and the other with a strong ($> 5 \times 10^{10}$ m^{-3}) ionization (orange lines) at an altitude of 247 km. Each median profile is shown by a solid black or dashed line.

when PsA patches were seen in WMI-558. The event selection was made by visual inspection using the quick-look viewer (http://pc115.seg20.nipr.ac.jp/www/AQVN/evs1.html). We examined the electron density data when a PsA was simultaneously detected by the WMI-580 in the following analysis method. First, the all-sky images were smoothed by 5 × 5 pixels to gain a signal-to-noise ratio. Figure 9a shows the keogram created from the smoothed all-sky images on February 18, 2018. The horizontal dashed line in Figure 9a represents the EISCAT radar observation point. The 558 nm emission intensity at this point is shown in Figure 9b. We conducted a wavelet transform, and the calculated power spectrum is given in Figure 9c. We excluded the data in the timings, shaded by gray in Figure 9, when the wavelet power in the frequency range from 2 to 40 s, which is a typical period of a PsA, was smaller than that of the red-noise level, with a confidence interval of 95% (Torrence & Compo, 1998). We also excluded the data in the timings shaded by red when the median electron temperature in the 240–270 km altitude range (black diamond and line in Figure 9f) was lower than its median value for an hour (red line in Figure 9f) to remove the influence of the electron density enhancement by the polar patches. Additionally, we excluded data when the local shadow height had an altitude of less than 400 km to remove the influence of the electron density enhancement by sunlight. Hence, we carefully selected the periods when the PsA was observed by the EISCAT radar and the all-sky imagers without the effects of polar patches and sunlit conditions, as indicated by the unshaded timings in Figure 9d.

Figure 10 shows the 272 extracted electron density profiles from the EISCAT data for 26 h with a temporal resolution of 1 min. There were two observation modes of the EISCAT radar during this period: one covered the altitude range from 76 to 282 km, and 124 profiles were obtained, as indicated by blue lines; the other mode covered the higher altitude range from 76 to 647 km, and 148 profiles were obtained, as indicated by orange lines. The median profile for each mode is shown by a solid black or dashed line. Focusing on the *F* region electron density obtained with

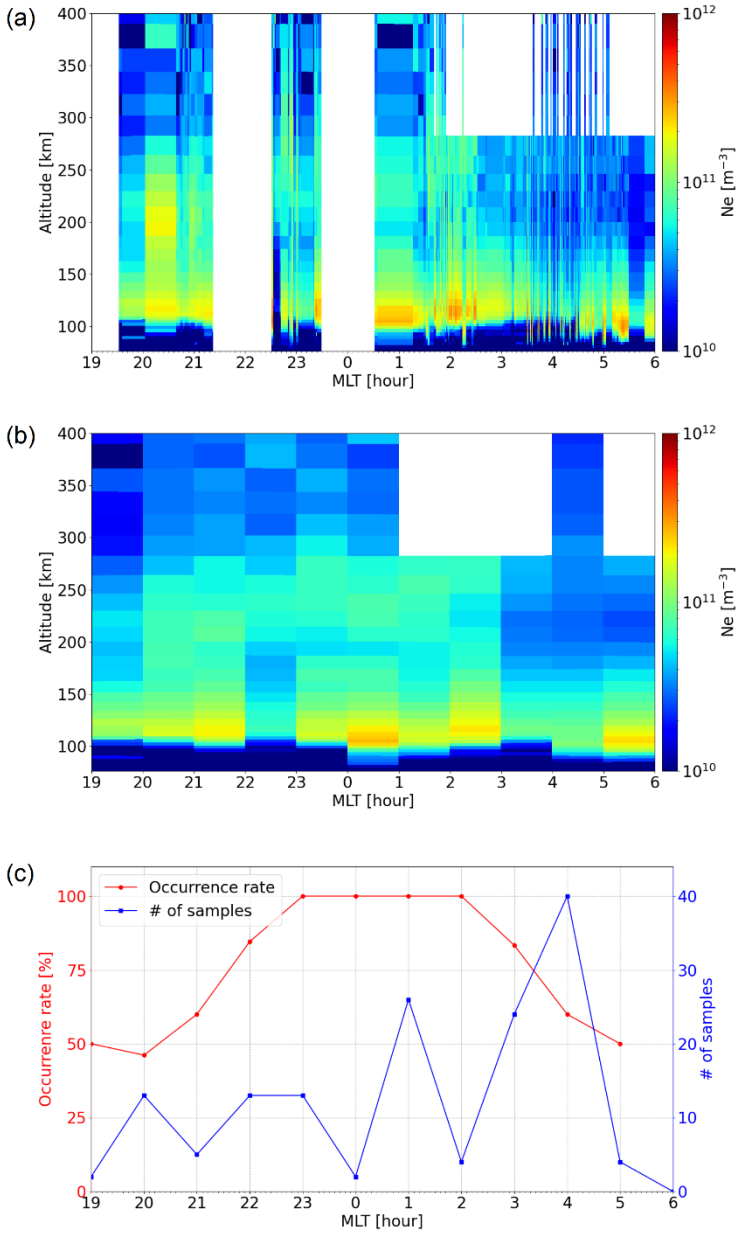

Figure 11 (a) MLT distribution of the extracted 272 electron-density height profiles. **(b)** Their median distribution during an hour. **(c)** The occurrence rate that the profile at each MLT had two peaks in the *E* and *F* region (red dot and line) and number of samples (blue dot and line).

the mode covering altitudes of 76–647 km, the median profile showed local maximums at two altitudes: 1.06×10^{11} m^{-3} at 114 km and 4.42×10^{10} m^{-3} at 247 km. We also saw the local minimum with 3.51×10^{10} m^{-3} at 187 km. The electron density estimated from the EISCAT data covering 76–282 km also tended to increase in the *F* region although it seemed difficult to identify the maximum of the electron density because of the coverage. Noteworthily, the electron height profile exhibited a double-peak structure, and therefore, we examined how many profiles had double peaks with a local minimum between them. We found that 112 profiles (76%) out of

the 148 profiles covering 76–647 km had such double peaks. This suggests that a PsA is accompanied by soft electron precipitations in most cases. We divided the 112 profiles that had double peaks into two cases; one with a weak ($\leq 5 \times 10^{10}$ m^{-3}) ionization (blue lines in Figure 10b), the other with a strong ($>5 \times 10^{10}$ m^{-3}) ionization (orange lines in Figure 10b) at an altitude of 247 km. The median profile for each case is shown by a solid black or dashed line. The numbers of profiles that had weak and strong *F* region ionization were 59 and 53, respectively. When the ionization in the *F* region was strong, the ionization in the *E* region was also strong.

Figure 11a shows the magnetic local time (MLT) distribution of the electron density profiles generated by sorting all of the 272 profiles in MLT. Figure 11b shows their hourly median distribution produced by allocating 1 h time slots, as in Figure 11a. Figure 11c shows the occurrence rate of double peaks (red dots and line) and the number of samples (blue dots and line) in the 1 h time slots. We note that the occurrence of double peaks exceeded 80% in the 22–3 MLT sector.

5 Summary and Discussion

We showed case studies, as well as statistical studies, of the electron density height profiles obtained with the EISCAT UHF radar, simultaneously obtained with PsA emission at 558 nm, to elucidate how often a PsA is accompanied by soft electron precipitation. From the statistical analysis, we found that 76% of electron density profiles had a double-peak structure with local enhancements in the ionospheric *E* (~110 km) and *F* (~250 km) regions. Using the global airglow (GLOW) model (Solomon et al., 1988), we estimated the height profiles of the ionization rate produced by the isotropic Maxwellian electrons, with a total energy flux of 1 erg cm^{-2} s^{-1} and characteristic energies in the range from 100 eV to 10 keV, in Tromsø at 1 UT on February 18, 2018 (Figure. 12). The GLOW model is available at http://download.hao.ucar.edu/pub/stans/glow. It is clear from this figure that the local enhancements at ~110 and ~250 km altitude could have been caused by the electron precipitation with energies of 10 keV and <100 eV, respectively, if the electron density enhancement was caused by the electron precipitation. It is reasonable that the upper atmospheric dynamics, such as ambipolar diffusion, were not considered in this study since the target was in the *E* and lower-*F* regions. From the electron height profile data for the 112 events when the double peak was observed, combined with the relationship between the precipitating electron energy and the ionization peak height, we estimated the electron energy for each peak altitude. We sorted these electron energy values into seven energy bins of 0.1, 0.2, 0.5, 1, 2, 5, and 10 keV. Figure 13 shows the occurrence rate histogram of the precipitating electron energies estimated for the *E* region peaks (blue bars) and the *F* region peaks (orange bars). We suggest from this result that 86% of the *E* region peaks were caused by precipitating electrons in the energy range from 500 eV to 5 keV, whereas 89% of the *F* region peaks were caused by electrons in the energy range below 100 eV. This is consistent with Tesema et al. (2020) who showed that the precipitating electrons had a low-energy peak at approximately 0.03–1 keV, besides a high-energy peak at ~10 keV.

The electron density enhancement in the *E* region in PsAs is caused by the precipitating electrons in the energy range from a few to a few tens of kiloelectron volts. Previous studies have shown that this relatively high-energy electron precipitation is generated by the pitch angle scattering with LBC waves near the magnetic equator (Kasahara et al., 2018). These relatively high-energy precipitating electrons cannot produce the enhancement of electron density in the *F* region. We

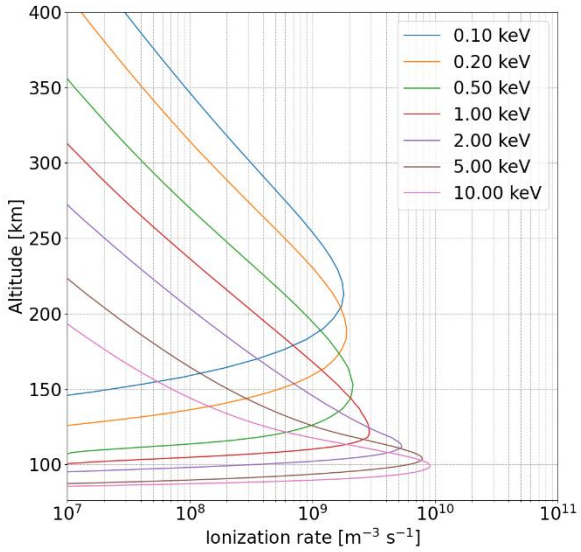

Figure 12 Ionization rate produced by isotropic Maxwellian electrons of total energy flux of 1 erg cm^{-2} s^{-1} and characteristic energies from 100 eV to 10 keV, using the GLOW model.

suggest that the electron density enhancement in the *F* region with electron temperature increase would be caused by precipitating electrons with energies lower than 1 keV, and these low-energy electrons are generated by UBC and/or ECH waves and the backscattered primary and secondary electrons in the opposite hemisphere (Evans et al., 1987; Fukizawa et al., 2018, 2020; Inan et al., 1992; Miyoshi et al., 2015). Figure 10b indicates that the electron density enhancements in the *E* and *F* regions have a positive correlation. This may imply that there is a positive correlation

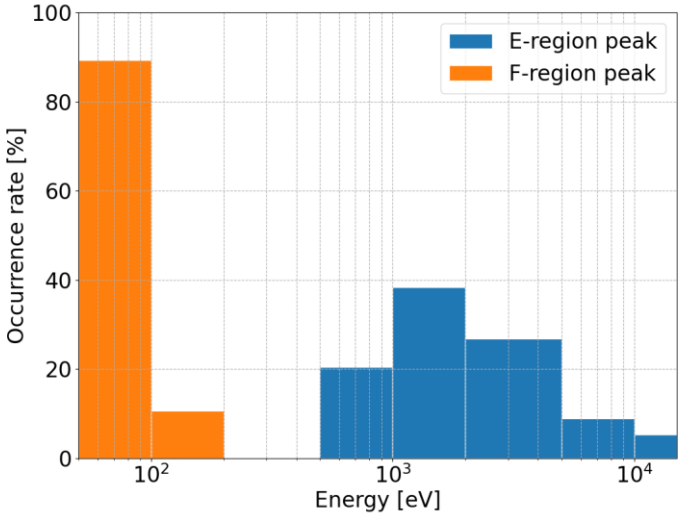

Figure 13 Occurrence rate of the *E*-region peak (blue bars) and of the *F*-region peak (orange bars) at the peak altitude of the ionization rate produced by electrons of characteristic energy, shown as the horizontal axis.

between each source mechanism or the LBC amplitude and the UBC and/or ECH amplitude at the magnetic equator. Note that the energy that contributes to enhancing the ionization rate at ~250 km altitude is lower than the typical cyclotron resonance energy of UBC and ECH waves. Whether UBC and ECH waves can scatter these low energy (<100 eV) electrons into a loss cone or not requires investigation in future work. Additionally, the flux of precipitating electrons backscattered in the opposite hemisphere, including secondary electrons, should be evaluated quantitatively.

The reduction of low-energy electron precipitation might easily be caused by the downward field-aligned potential drop in the downward field-aligned current region associated with PsAs (Samara et al., 2015) and the lack of excitation of UBC and/or ECH waves in the source region of the magnetic equator.

As shown in Figure 11c, the occurrence rate of the *F* region electron density peak event in the hourly MLT exceeded 80% in the 22–3 MLT sector (Figure 11c). Ni et al. (2017) reported that strong (>1.0 mV m^{-1}) ECH waves are also frequently excited at the magnetic equator (|MLAT| < 3°) in approximately the same MLT range. By contrast, the UBC wave intensity is strong in a wider range from 20 to 11 MLT sectors (Meredith et al., 2012). Likely, the appearance of a UBC is not consistent with the result of the occurrence of an *F* region electron density peak event, showing the decrease of occurrence in the morning sectors greater than 3 MLT (see Figure 11c). Also note that the MLT range of the occurrence rate of the *F* region electron density peak is approximately consistent with that of the polar patches observed in Ny-Ålesund, Norway (78.9°N, 12°E; 76°MLAT) (Moen et al., 2007). Although we set the threshold of electron temperature to remove the influence of electron density enhancement by polar patches in the statistical analysis, we may not have been able to completely remove it. The identification of the generation process of the *F* region electron density enhancement associated with PsAs will be conducted by coordinated ground–satellite observations in the future.

One of the unsolved questions for PsAs is what determines their shapes. The low-energy electron precipitation in PsAs, which are suggested in this study, may contribute to a change in the spatial structure of the plasma density or the growth rate of the driver of the PsAs (chorus and ECH waves) in the magnetosphere by the outflowing of the ionospheric plasma into the magnetosphere.

Acknowledgments, Samples, and Data

This work was performed using data from the National Institute of Polar Research (NIPR). The electron density and temperature data used in this study are a part of the EISCAT database in the NIPR, which is available at http://polaris.nipr.ac.jp/~eiscat/eiscatdata/. EISCAT is an international association supported by research organisations in China (CRIRP), Finland (SA), Japan (NIPR), Norway (NFR), Sweden (VR), and the United Kingdom (UKRI). The all-sky images used in this study are available at http://pc115.seg20.nipr.ac.jp/www/AQVN/evs1.html. The spectrograph data are available at http://ttt01.cei.uec.ac.jp/sg01/. The SPEDAS software (Angelopoulos et al., 2019) was used for the data analysis in this study. The first author is a Research Fellow of the Japanese Society for the Promotion of Science (DC) and is supported by JSPS KAKENHI Grant Number JP20J11829. Y.O. and K.H. are supported by JSPS KAKENHI Grant Number JP15H05747. T.T.T. and K.H. are supported by JSPS KAKENHI Grant Number JP20K20940.

References

Evans, D. S., Davidson, G. T., Voss, H. D., Imhof, W. L., Mobilia, J., & Chiu, Y. T. (1987). Interpretation of electron spectra in morningside pulsating aurorae. *Journal of Geophysical Research: Space Physics, 92*(A11), 12295–12306. https://doi.org/10.1029/JA092iA11p12295

Folkestad, K., Hagfors, T., & Westerlund, S. (1983). EISCAT: An updated description of technical characteristics and operational capabilities. *Radio Science*, *18*(6), 867–879. https://doi.org/10.1029/RS018i006p00867

Fukizawa, M., Sakanoi, T., Miyoshi, Y., Hosokawa, K., Shiokawa, K., & Katoh, Y. (2018). Electrostatic electron cyclotron harmonic waves as a candidate to cause pulsating auroras. *Geophysical Research Letters*, *45*(12), 661–668. https://doi.org/10.1029/2018GL080145

Fukizawa, M., Sakanoi, T., Miyoshi, Y., Kazama, Y., Katoh, Y., Kasahara, Y., et al. (2020). Pitch-angle scattering of inner magnetospheric electrons caused by ECH waves obtained with the Arase satellite. *Geophysical Research Letters*, *47*(23), 1–9. https://doi.org/10.1029/2020GL089926

Grono, E., & Donovan, E. (2018). Differentiating diffuse aurora based on phenomenology. *InAnnales Geophysicae*, *36*(3), 891–898. https://doi.org/10.5194/angeo-36-891-2018

Horne, R. B., Thorne, R. M., Meredith, N. P., & Anderson, R. R. (2003). Diffuse auroral electron scattering by electron cyclotron harmonic and whistler mode waves during an isolated substorm. *Journal of Geophysical Research: Space Physics*, *108*(A7), 1–12. https://doi.org/10.1029/2002JA009736

Inan, U. S., Chiu, Y. T., & Davidson, G. T. (1992). Whistler-mode chorus and morningside aurorae. *Geophysical Research Letters*, *19*(7), 653–656. https://doi.org/10.1029/92GL00402

Kasahara, S., Miyoshi, Y., Yokota, S., Mitani, T., Kasahara, Y., Matsuda, S., et al. (2018). Pulsating aurora from electron scattering by chorus waves. *Nature*, *554*(7692), 337–340. https://doi.org/10.1038/nature25505

Liang, J., Donovan, E., Jackel, B., Spanswick, E., & Gillies, M. (2016). On the 630nm red-line pulsating aurora: Red-line Emission Geospace Observatory observations and model simulations. *Journal of Geophysical Research: Space Physics Research*, *121*, 7988–8012. https://doi.org/10.1002/2016JA022901

Liang, J., Donovan, E., Reimer, A., Hampton, D., Zou, S., & Varney, R. (2018). Ionospheric Electron heating associated with pulsating auroras: joint optical and PFISR observations. *Journal of Geophysical Research: Space Physics*, *123*(5), 4430–4456. https://doi.org/10.1029/2017JA025138

McEwen, D. J., Yee, E., Whalen, B. A., & Yau, A. W. (1981). Electron energy measurements in pulsating auroras. *Canadian Journal of Physics*, *59*(8), 1106–1115. https://doi.org/10.1139/p81-146

Meredith, N. P., Horne, R. B., Sicard-Piet, A., Boscher, D., Yearby, K. H., Li, W., & Thorne, R. M. (2012). Global model of lower band and upper band chorus from multiple satellite observations. *Journal of Geophysical Research: Space Physics*, *117*(10), 1–14. https://doi.org/10.1029/2012JA017978

Miyoshi, Y., Saito, S., Seki, K., Nishiyama, T., Kataoka, R., Asamura, K., et al. (2015). Relation between energy spectra of pulsating aurora electrons and frequency spectra of whistler-mode chorus waves. *Journal of Geophysical Research: Space Physics*, 1–9. https://doi.org/10.1002/2015JA021562.

Moen, J., Gulbrandsen, N., Lorentzen, D. A., & Carlson, H. C. (2007). On the MLT distribution of F region polar cap patches at night. *Geophysical Research Letters*, *34*(14), 7–10. https://doi.org/10.1029/2007GL029632

Ni, B., Gu, X., Fu, S., Xiang, Z., & Lou, Y. (2017). A statistical survey of electrostatic electron cyclotron harmonic waves based on THEMIS FFF wave data. *Journal of Geophysical Research: Space Physics*, *122*(3), 3342–3353. https://doi.org/10.1002/2016JA023433

Nishimura, Y., Bortnik, J., Li, W., Thorne, R. M., Lyons, L. R., Angelopoulos, V., et al. (2010). Identifying the driver of pulsating aurora. *Science*, *330*(6000), 81–84. https://doi.org/10.1126/science.1193186

Ogawa, Y., Tanaka, Y., Kadokura, A., Hosokawa, K., Ebihara, Y., Motoba, T., et al. (2020). Development of low-cost multi-wavelength imager system for studies of aurora and airglow. *Polar Science*, *23*(April 2019). https://doi.org/10.1016/j.polar.2019.100501

Oyama, S., Miyoshi, Y., Shiokawa, K., Kurihara, J., Tsuda, T. T., & Watkins, B. J. (2014). Height-dependent ionospheric variations in the vicinity of nightside poleward expanding aurora after substorm onset. *Journal of Geophysical Research: Space Physics*, *119*, 4146–4156. https://doi.org/10.1002/2013JA019704

Oyama, Shin ichiro, Tsuda, T. T., Hosokawa, K., Ogawa, Y., Miyoshi, Y., Kurita, S., et al. (2018). Auroral molecular-emission effects on the atomic oxygen line at 777.4 nm. *Earth, Planets and Space*, *70*(1), 0–6. https://doi.org/10.1186/s40623-018-0936-z

Saito, Y., Machida, S., Hirahara, M., Mukai, T., & Miyaoka, H. (1992). Rocket observation of electron fluxes over a pulsating aurora. *Planetary and Space Science*, *40*(8), 1043–1054. https://doi.org/10.1016/0032-0633(92)90033-K

Samara, M., Michell, R. G., & Redmon, R. J. (2015). Low-altitude satellite measurements of pulsating auroral electrons. *Journal of Geophysical Research A: Space Physics*, *120*(9), 8111–8124. https://doi.org/10.1002/2015JA021292

Sandahl, I., Eliasson, L., & Lundin, R. (1980). Rocket observations of precipitating electrons over a pulsating aurora. *Geophysical Research Letters*, *7*(5), 309–312. https://doi.org/10.1029/GL007i005p00309

Smith, M. J., Bryant, D. A., & Edwards, T. (1980). Pulsations in auroral electrons and positive ions. *Journal of Atmospheric and Terrestrial Physics*, *42*(2), 167–178. https://doi.org/10.1016/0021-9169(80)90077-X

Solomon, S. C., Hays, P. B., & Abreu, V. J. (1988). The auroral 6300 Å emission : observations and modeling. *J. Geophys. Res.*, *93*, 9867–9882. https://doi.org/10.1029/JA093iA09p09867

Tao, X., Thorne, R. M., Li, W., Ni, B., Meredith, N. P., & Horne, R. B. (2011). Evolution of electron pitch angle distributions following injection from the plasma sheet. *Journal of Geophysical Research: Space Physics*, *116*(4), 1–8. https://doi.org/10.1029/2010JA016245

Tesema, F., Partamies, N., Tyssøy, H. N., Kero, A., & Smith-Johnsen, C. (2020). Observations of electron precipitation during pulsating aurora and its chemical impact. *Journal of Geophysical Research: Space Physics*, *125*(6), e2019JA027713. https://doi.org/10.1029/2019JA027713

Thorne, R. M., Ni, B., Tao, X., Chen, L., Li, W., Meredith, N. P., et al. (2013). Correction to "Resonant scattering of plasma sheet electrons leading to diffuse auroral precipitation: 1. Evaluation for electrostatic electron cyclotron harmonic waves," "Resonant scattering of plasma sheet electrons leading to diffuse auroral precipitation: 2. Evaluation for whistler mode chorus waves," and "Evolution of pitch angle distributions following injection from the plasma sheet". *Journal of Geophysical Research: Space Physics*, *118*, 839–842. https://doi.org/10.1002/jgra.50154

Torrence, C., & Compo, G. P. (1998). A practical guide to wavelet analysis. *Bulletin of the American Meteorological Society*, *79*(1), 61–78. https://doi.org/10.1175/1520-0477(1998)079<0061:APGTWA>2.0.CO;2

Tsuda, T. T., Li, C., Hamada, S., Hosokawa, K., Oyama, S. I., Nozawa, S., et al. (2020). OI 630.0-nm and N2 1PG emissions in pulsating aurora events observed by an optical spectrograph at Tromsø, Norway. *Journal of Geophysical Research: Space Physics*, *125*(12), 1–11. https://doi.org/10.1029/2020JA028250

Whalen, B. A., Miller, J. R., & McDiarmid, I. B. (1971). Energetic particle measurements in a pulsating aurora. *NACA TN No. 1326*, *76*(4), 978–986. https://doi.org/10.1029/JA076i004p00978

Yamamoto, T. (1988). On the Temporal fluctuations of pulsating auroral luminosity. *Journal of Geophysical Research*, *93*(A2), 897–911. https://doi.org/10.1029/JA093iA02p00897